ADVANCED MATERIALS
www.advmat.de

Reviving Oxygen Evolution Electrocatalysis of Bulk La–Ni Intermetallics via Gaseous Hydrogen Engineering

Ziliang Chen, Hongyuan Yang, Stefan Mebs, Holger Dau, Matthias Driess, Zhaowu Wang, Zhenhui Kang,* and Prashanth W. Menezes**

A hydrogen processing strategy is developed to enable bulk $LaNi_5$ to attain high activity and long-term stability toward the electrocatalytic oxygen evolution reaction (OER). By a combination of in situ Raman and quasi in situ X-ray absorption (XAS) spectra, secondary-electron-excited scanning transmission electron microscopy (STEM) patterns as well as the Rietveld method and density functional theory (DFT) calculations, it is discovered that hydrogen-induced lattice distortion, grain refinement, and particle cracks dictate the effective reconstruction of the $LaNi_5$ surface into a porous hetero-nanoarchitecture composed of uniformly confined active γ-NiOOH nanocrystals by $La(OH)_3$ layer in the alkaline OER process. This significantly optimizes the charge transfer, structural integrity, active-site exposure, and adsorption energy toward the reaction intermediates. Benefiting from these merits, the overpotential (322 mV) at 100 mA cm^{-2} for the hydrogen-processed OER catalyst deposited on nickel foam is reduced by 104 mV as compared to the original phase. Notably, it exhibits remarkable stability for 10 days at an industrial-grade current density of more than 560 mA cm^{-2} in alkaline media.

1. Introduction

The thermodynamically uphill and sluggish kinetics of oxygen evolution reaction (OER) has been regarded as a bottleneck to realize efficient hydrogen production via electrochemical water splitting.[1–4] Therefore, the design of highly active, cost-effective, and durable electrocatalysts is of prime importance to economically and effectively drive OER.[5–9] To tackle this challenge, recently, intermetallic compounds based on non-noble transition metals (TM: Fe, Co, Ni, Mn) have gained particular attention owing to their low resistivities, tunable compositions, and unique crystal structures.[10–15] Current research on the intermetallics-based OER electrocatalysts concentrates on alloying TMs and metalloids (e.g., B, Si, Ge, As) or lean metals (e.g., Al, Ga, Sn, Bi).[16–25] Within these intermetallics, the TM species strictly in situ converted into active TM (oxy)hydroxides while the nonmetals mostly leached out of the structure during alkaline OER, resulting in the formation of active nanodomains and thus an enhancement of catalytic activity.[17,18] Furthermore, in most cases, the inner part of bulk intermetallics could be retained well albeit the surface undergoes restructuring, leading to the generation of unique core–shell architecture with high conductivity.[21] Alternatively, the intermetallics are also known to transform completely at applied OER potentials depending on the size and the type of nonmetals in the structure by forming porous bulk-active catalysts.[15] Despite the appealing progress that has been achieved

Z. Chen, Z. Kang
Institute of Functional Nano and Soft Materials (FUNSOM)
Jiangsu Key Laboratory for Carbon-Based Functional Materials and Devices
Soochow University
Suzhou 215123, P. R. China
E-mail: zlchen@suda.edu.cn; zhkang@suda.edu.cn

H. Yang, M. Driess, P. W. Menezes
Department of Chemistry
Metalorganics and Inorganic Materials
Technische Universität Berlin
Straße des 17 Juni 135, Sekr. C2, 10623 Berlin, Germany
E-mail: prashanth.menezes@helmholtz-berlin.de

S. Mebs, H. Dau
S Department of Physics
Free University of Berlin
Arnimallee 14, 14195 Berlin, Germany

Z. Wang
School of Physics and Engineering, Longmen laboratory
Henan University of Science and Technology
Luoyang 471023, P. R. China

P. W. Menezes
Materials Chemistry Group for Thin Film Catalysis–CatLab
Helmholtz-Zentrum Berlin für Materialien und Energie
Albert-Einstein-Str. 15, 12489 Berlin, Germany

The ORCID identification number(s) for the author(s) of this article can be found under https://doi.org/10.1002/adma.202208337.

DOI: 10.1002/adma.202208337

in the relevant research field, it is still of great interest to search for novel intermetallics for efficient alkaline OER and to reveal their active structures, understand their OER mechanism as well as to derive their composition–(micro)structure–performance correlation.

Rare earth metal and TM can form a series of interesting intermetallic compounds with the chemical formula of AB_x (A = rare-earth metal, B = TM, x = 2, 3, 3.5, 4, 5).[26,27] However, there are barely any studies on their OER activity, and their related OER mechanism still remains elusive. Among these AB_x, $LaNi_5$-based intermetallics are structurally interesting as well as known to be classical hydrogen storage materials.[28,29] As a pioneering work, Shi et al. recently synthesized nickel foam (NF)-supported $LaNi_5$ honeycomb by a long-term potentiostatic electrolysis in molten salt under an Ar-protected glovebox, which delivered an overpotential of 347 mV at 100 mA cm^{-2} during OER in 1.0 M KOH.[30] Despite this appealing result, an admirable OER performance concurrently integrating the high activity and long-stability at industrial current density (500 mA cm^{-2}) is still lacking. Furthermore, the practical application of such catalysts is probably limited by the harsh and tedious conditions involved in the preparation process. Since the OER performance of (pre)catalysts is highly dependent on their microstructure,[31–33] one may consider employing the conventional mechanical ball milling to optimize the morphology and crystal structure of the bulk intermetallics for improving the activity. However, this method may have demerits including sample pollution and oxidation as well as the serious loss of raw materials. To address this challenge, it is highly desired to explore a simple, effective, and controllable method to enable $LaNi_5$ to achieve an outstanding OER performance at industrial current density.

Intriguingly, $LaNi_5$ can undergo the reversible hydrogen absorption and desorption cycle under ambient conditions by the insertion and de-insertion of hydrogen atoms in the lattice interstitials. Furthermore, the hydrogen-cycle-induced volume variation of $LaNi_5$ can reach up to as high as 200%,[34,35] which inevitably modifies the morphology and microstructure. Based on this premise, an open question can naturally be raised as to whether this hydrogen-cycling-induced structural change can improve the OER activity and stability of $LaNi_5$. So far, it is well known that metalloid and lean metal species severely leach during alkaline OER forming TM oxyhydroxide nanodomains that eventually aggregate with prolonged catalytic reaction, leading to a decrease in the activity and stability. Therefore, the other important question to address here is how rare-earth metals (such as La) behave under prolonged OER conditions. Do such rare-earth metals leach out of the structure or would they prefer to form oxide or hydroxide precipitants,[36] which can probably serve as a barrier or a layer to suppress the aggregation of the formed TM oxyhydroxides nanodomains, and thereby to enable good preservation of their activity and stability?

Bearing the above-mentioned questions in mind, herein, bulk $LaNi_5$ prepared by melting followed by annealing was used as a starting material for this contribution. We treated $LaNi_5$ having an average particle size of 38 μm by repetitive hydrogen absorption and desorption cycles. The repeated lattice volume variation produced by multiple hydrogen absorption and desorption cycles intensified crystal defects, lattice strain, grain refinement, and particle cracks, which greatly improved the exposure of metal sites. Furthermore, through a series of secondary-electron-excited scanning transmission electron microscopy (STEM), quasi in situ X-ray absorption (XAS), and in situ Raman spectroscopy characterizations, we discovered that in the OER process, unlike semimetals and metalloids, rare-earth La was not prone to leach and got dissolved in the electrolyte, but rather formed $La(OH)_3$ barrier on the particle surface. This barrier uniformly confined the transformed ultrafine γ-NiOOH nanoparticles, generating a porous core–shell structure with the remaining internal part of $LaNi_5$ (γ-NiOOH/$La(OH)_3$/$LaNi_5$). Owing to the confinement and coupling of $La(OH)_3$, the aggregation of these active γ-NiOOH nanoparticles was inhibited, and they were homogeneously and sufficiently exposed to the electrolyte, ensuring abundant accessible active sites, accelerated charge transfer, rapid mass diffusion, high structural stability as well as the optimized adsorption ability toward intermediates. Benefiting from these advantages, the overpotential at 100 mA cm^{-2} for the optimized electrocatalyst deposited on nickel foam (NF) was only 322 mV, which was reduced by 104 mV compared with that for the original phase. Moreover, the hydrogen-processed electrocatalyst exhibited ultrahigh OER stability for 10 days at industrial-grade current density (≈560 mA cm^{-2}) in ambient conditions.

2. Results and Discussion

The as-prepared bulk $LaNi_5$ powder was cycled in the gaseous hydrogen atmosphere at room temperature, by which particle cracks, grain refinement as well as lattice distortion were triggered or increased, as schematically illustrated in **Figure 1**. The initial hydrogen absorption amount for $LaNi_5$ could reach up to 1.40 wt% (Figure S1, Supporting Information), which corresponded to the formation of hydride phase $LaNi_5H_{6.1}$, being in good agreement with previous reports.[28,29] The formation of such a hydride phase has been demonstrated to incur an anisotropic volume expansion as high as ≈200% owing to the insertion of hydrogen atoms into the lattice interstitials along the *c*-axis.[34,35] With further desorption, the lattice was remarkably contracted along the opposite direction. Because of the severe lattice expansion and contraction, the lattice distortion occurred after cycling. According to the refinement results of X-ray diffraction (XRD) patterns (**Figure 2**a,b; Figure S2, Table S1, Supporting Information), ≈0.35% of lattice volume expansion resulted after the initial cycle. Upon prolonging the hydrogen cycle to 100 times, the lattice distortion was further enhanced but to a quite small magnitude (Figure S2c, Supporting Information). The lattice strain was also apparently increased by 2.4% after the initial cycle, whereas it was only increased by 0.4% from the initial cycle to the 100th one (Figure 2b). It is widely accepted that the lattice strain directly correlates with the lattice defects.[27,37] Furthermore, the larger the lattice strain is, the higher the degree of lattice defects usually present.[27,37] Based on this fact, it could rationally be concluded that hydrogen processing could effectively introduce lattice defects, which is believed to be conducive to exposing active sites and increasing the reaction activity of metal species.[38,39] Note that the hydrogen processing kept the composition unchanged

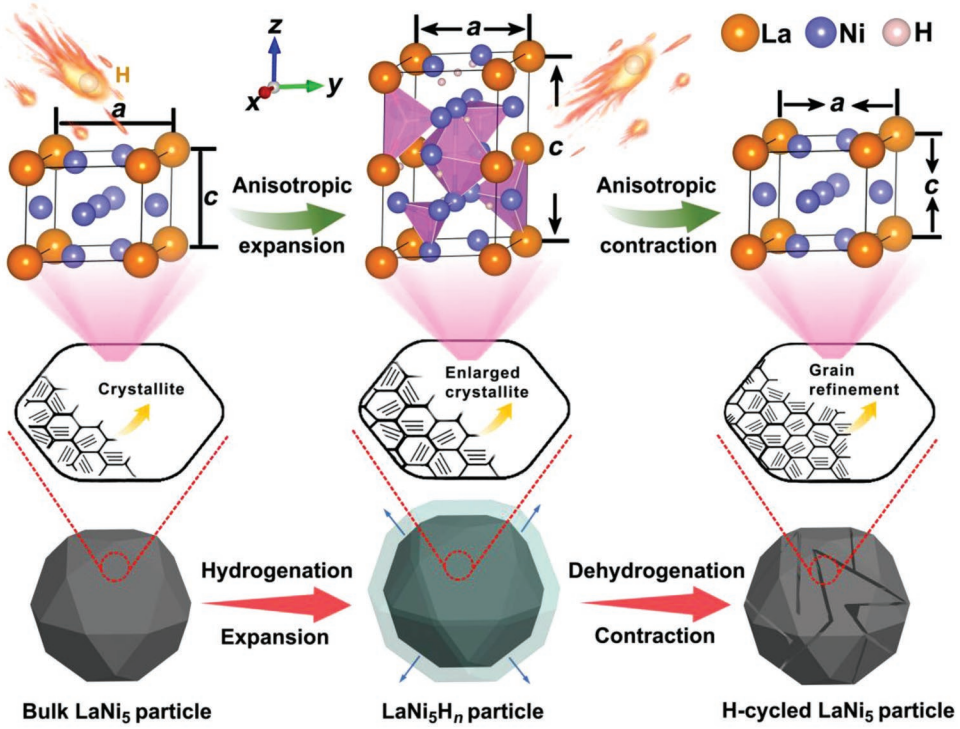

Figure 1. Schematic illustration for the hydrogen processing strategy toward the optimization of bulk $LaNi_5$.

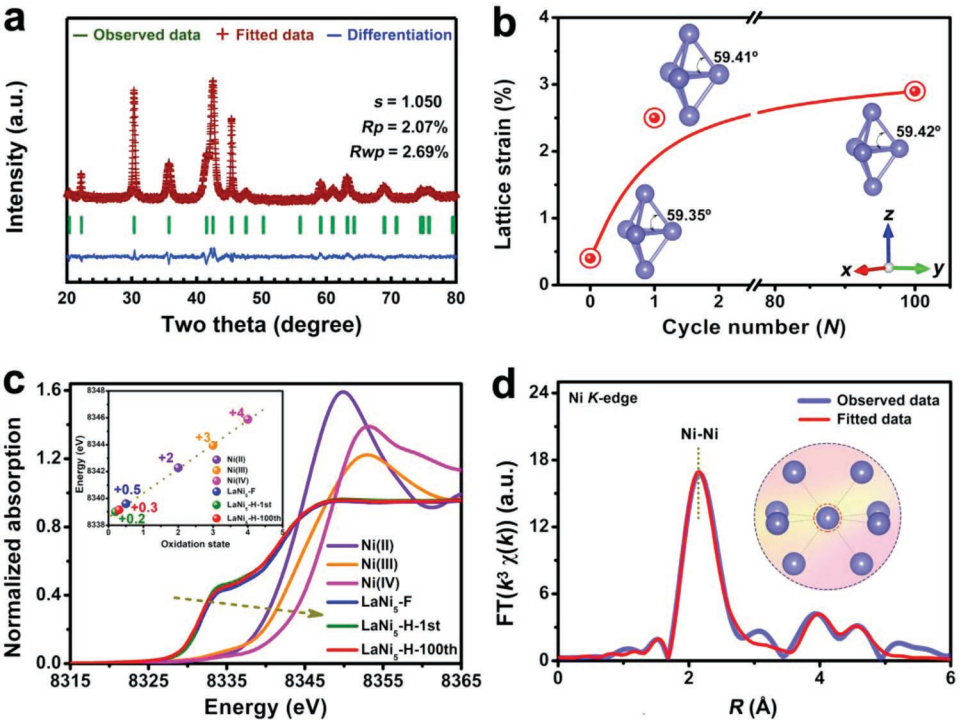

Figure 2. a) Rietveld refinement of XRD pattern for the $LaNi_5$-H-100th sample. b) Lattice strain variation of the $LaNi_5$ compound against the hydrogen adsorption–desorption cycle. c) XANES spectra of Ni *K*-edge in $LaNi_5$-F, $LaNi_5$-H-1st, $LaNi_5$-H-100th compounds, together with standard Ni(II), Ni(III) and Ni(IV) samples for reference. d) Fitted EXAFS spectra of Ni *K*-edge in $LaNi_5$-H-100th compound. Inset in (d): the structural configuration of the Ni center coordinated with the Ni atoms in the first shell. Ni(II), Ni(III), and Ni(IV) represent the NiO, NiO_2Li and $Ni(K_2(H_2IO_6)_2$ reference samples, respectively.

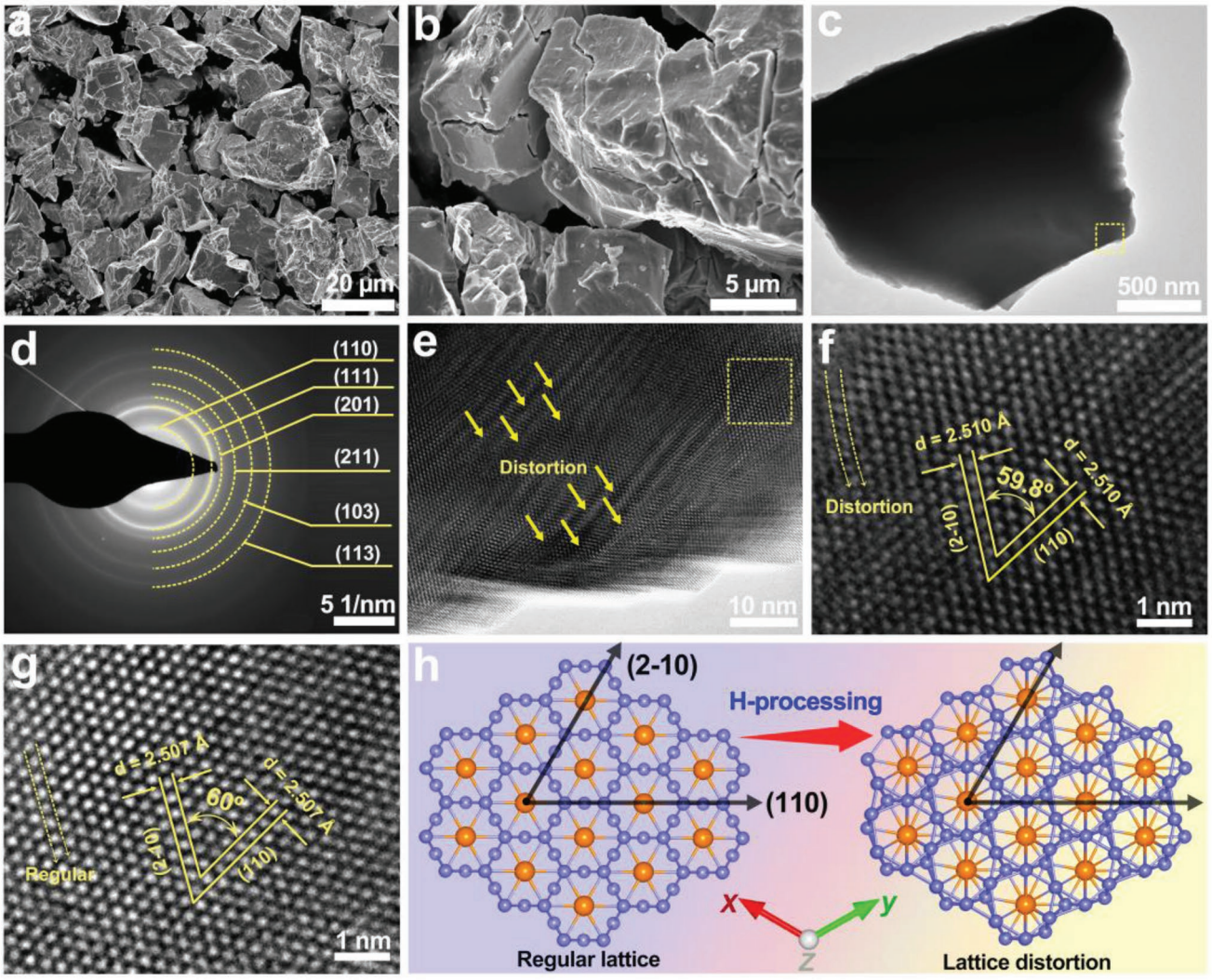

Figure 3. a,b) FESEM images, c) TEM image and d) corresponding SAED pattern, and e,f) HRTEM images of $LaNi_5$-H-100th compound. g) HRTEM image of $LaNi_5$-F. h) Schematic illustration for hydrogen-processing-induced lattice distortion of $LaNi_5$.

(Table S2, Supporting Information). On the other hand, the average crystallite size of $LaNi_5$ was reduced from 134 to 85 nm after the initial cycle, and 8 nm was further deceased from the initial cycle to the 100th one (Figure S2d, Supporting Information). Such a grain refinement could generate abundant grain boundaries, which is also beneficial for the exposure of active metal species.[40,41] These results strongly indicated that strain and average size could be controllably tuned by hydrogen cycling and to an even greater extent in the first cycle itself. The Ni *K*-edge X-ray absorption spectra (XAS) of these materials are provided in Figure 2c. The extracted X-ray absorption near edge structure (XANES) showed that the chemical state of Ni species for all three materials was quite close to the metallic one (Inset in Figure 2c). The corresponding extended X-ray absorption fine structure (EXAFS) pattern further confirmed the phase structure of $LaNi_5$ in all three samples (Figure 2d; Figure S3, Table S3, Supporting Information).

Field-emission scanning electron microscopy (FESEM) images displayed that in comparison with the fresh $LaNi_5$ compound ($LaNi_5$-F), a number of cracks were generated on the particle surface after hydrogenation and dehydrogenation cycles (**Figure 3**a,b; Figure S4, Supporting Information), which was thought to be favorable to exposing active sites and accelerating mass transport. Selected-area electron diffraction (SAED) profile (Figure 3d) recorded from the TEM image (Figure 3c) for the 100th hydrogen-cycled $LaNi_5$ ($LaNi_5$-H-100th) confirmed the $LaNi_5$ phase structure. Further high-resolution TEM (HRTEM) images clearly showed lattice distortions in the $LaNi_5$-H-100th sample (Figure 3e,f). Such lattice distortion was also apparently identified in $LaNi_5$ after the 1st hydrogen cycle ($LaNi_5$-H-1st) (Figure S5, Supporting Information) but was in a much more relaxed state for the fresh $LaNi_5$ phase (Figure 3g; Figure S6, Supporting Information). As shown in Figure 3f, the lattice fringes with distances of 2.510 and 2.510 Å were assigned to (110) and (2–10) facets of the $LaNi_5$ phase, respectively, from which an intersection angle of ≈59.8° was obtained. This lattice distance and intersection angle were slightly different from the corresponding ones observed for the as-prepared $LaNi_5$-F

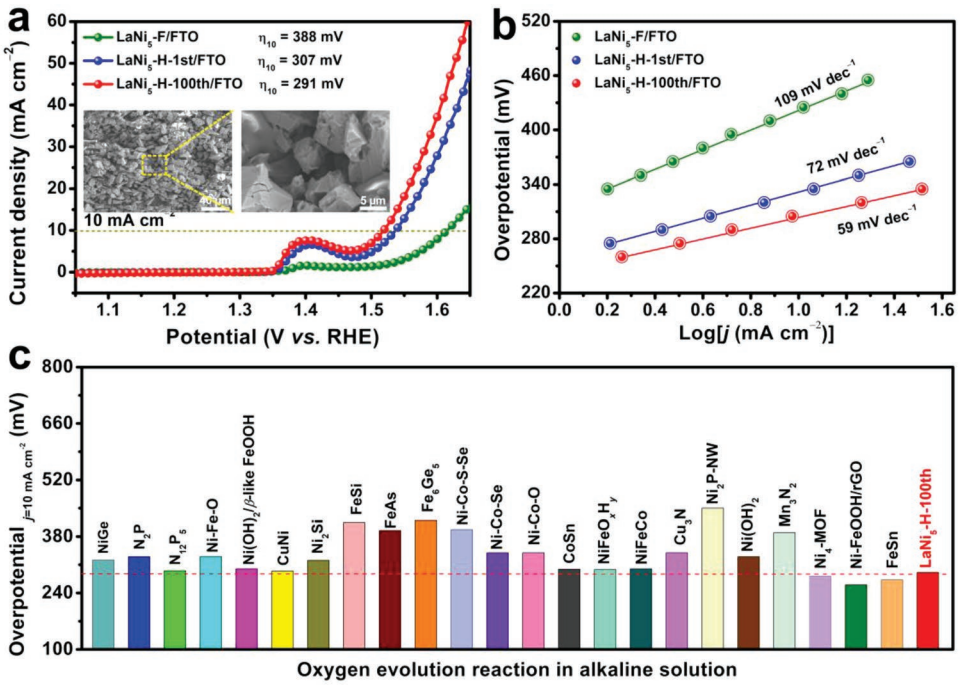

Figure 4. a) LSV curves and b) Tafel slopes of $LaNi_5$-F/FTO, $LaNi_5$-H-1st/FTO, and $LaNi_5$-H-100th/FTO electrodes in 1.0 M KOH. c) Comparison of the activity of $LaNi_5$-H-100th/FTO electrode with recently reported FTO-supported TM-based electrodes. Inset in (a): FESEM images of $LaNi_5$-H-100th deposited on FTO.

(Figure 3g), which was due to the hydrogen-cycling-induced lattice strain, as schematically shown in Figure 3h. The high-angle annular dark-field (HAADF)-STEM image and corresponding mapping results verified the uniform distribution of La and Ni metal species (Figure S7, Supporting Information) and were similar to those for $LaNi_5$-F (Figure S6, Supporting Information) and $LaNi_5$-H-1st (Figure S5, Supporting Information). The above phenomena demonstrated again that cyclic hydrogenation and dehydrogenation induced the morphology and structural modification while keeping the composition unchanged. Moreover, for comparison, the pure Ni powders (denoted Ni-F) were prepared by a similar procedure as that of the $LaNi_5$-F powder and the obtained Ni-F powders were further subjected to 100 hydrogen absorption and desorption cycles under identical conditions to obtain the analog Ni-H-100th sample. Compared with $LaNi_5$-F, the hydrogen absorption amount for Ni-F was quite low (≈0.04 wt%) (Figure S1, Supporting Information), which could be attributed to the unfavorable thermodynamics under the condition of 298 K and 5 MPa H_2.[42,43] The Rietveld refinement of XRD patterns and FESEM results showed that the lattice strain, lattice volume, crystallite size as well as the surface cracks for Ni-F only changed slightly after hydrogen processing (Figures S8 and S9, Table S1, Supporting Information). This phenomenon also suggests that, unlike traditional metals and alloys, the microstructure of hydrogen storage alloys based on the rare earth-transition metal system can be effectively modified through unique strategies such as gaseous hydrogen engineering, thereby offering a new avenue to optimize the OER performance.

Since the morphology and microstructure were modified through hydrogen processing, we then targeted the alkaline OER to evaluate the catalytic performance of $LaNi_5$-H-100th, together with $LaNi_5$-F and $LaNi_5$-H-1st for comparison. These powders were first deposited onto fluorine-doped tin oxide (FTO) with the same mass loading amount (1.5 mg cm^{-2}). Both the phase structure and morphology for $LaNi_5$-H-100th were retained after depositing on FTO ($LaNi_5$-H-100th/FTO) (Inset in **Figure 4**a; Figures S10 and S11, Supporting Information). The linear polarization curve showed the poor activity of $LaNi_5$-F deposited on FTO ($LaNi_5$-F/FTO), which delivered the overpotential as high as 388 mV (η_{10}) at 10 mA cm^{-2} (Figure 4a). Remarkably, only after one cyclic hydrogenation and dehydrogenation treatment, the overpotential was reduced by 81 mV at 10 mA cm^{-2}, and it was further decreased to 291 mV after 100 hydrogenation and dehydrogenation cycles. Particularly, such activity optimization tendency was more apparent at larger current densities. Note that the pristine FTO exhibited inert OER activity (Figure S12, Supporting Information), meaning it has a little contribution to the whole OER activity of the $LaNi_5$-based electrodes. The Tafel slope analysis based on the steady-state measurements showed that $LaNi_5$-H-100th bear a smaller value (59 mV dec^{-1}) than those of $LaNi_5$-F (109 mV dec^{-1}) and $LaNi_5$-H-1st (72 mV dec^{-1}) (Figure 4b), indicating that it had the best reaction kinetics within a certain potential range. Moreover, the superior performance of $LaNi_5$-H-100th ranks it at the top level among the previously reported intermetallics and Ni-based electrocatalysts on FTO (Figure 4c; Table S4, Supporting Information).

To better unveil the effect of hydrogen processing on the activity, electrochemical impedance spectra (EIS) were determined and the results showed that the charge transfer ability for $LaNi_5$ was strikingly improved upon performing hydrogen

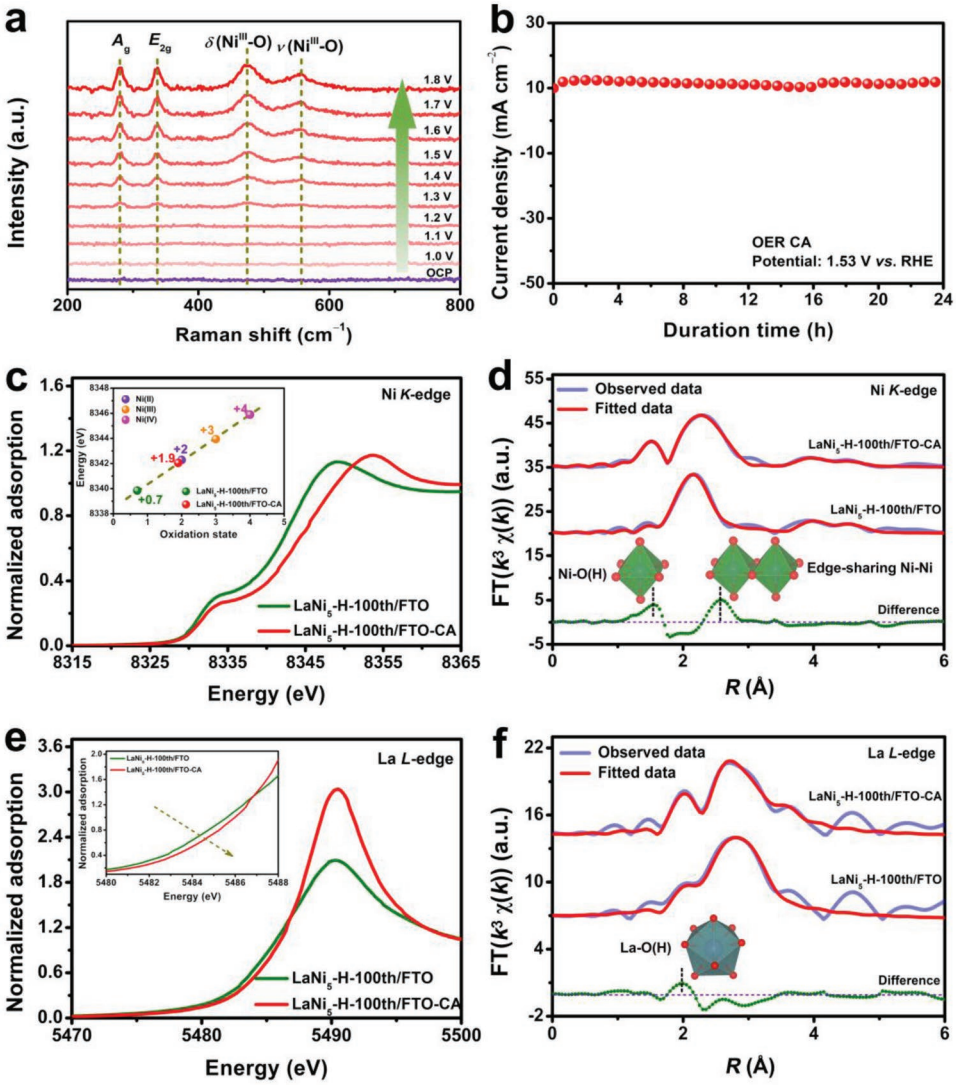

Figure 5. a) In situ Raman spectra of $LaNi_5$-H-100th starting from 1.0 V vs RHE with increasing the potential in 0.1 V intervals (the first line close to the graph bottom represents the signal from the as-prepared sample at the open circuit potential (OCP)). b) CA curve of $LaNi_5$-H-100th/FTO electrode in 1.0 M KOH. c) Comparison of XANES spectra of Ni *K*-edge in $LaNi_5$-H-100th/FTO electrode before and after CA test. d) Fitted EXAFS spectra of Ni *K*-edge in $LaNi_5$-H-100th/FTO electrode before and after CA test. e) Comparison of XANES spectra of La *L*-edge in $LaNi_5$-H-100th/FTO electrode after CA test. f) Fitted EXAFS spectra of La *L*-edge in $LaNi_5$-H-100th/FTO electrode after CA test. Ni(II), Ni(III), and Ni(IV) represent the NiO, NiO_2Li and $Ni(K_2(H_2IO_6)_2$ reference samples, respectively. The difference curve shown in (d,f) is achieved by subtracting the EXAFS spectrum FT amplitude of $LaNi_5$-H-100th/FTO before CA from that of after CA.

cycles (Figure S13, Supporting Information), which meant the optimization of the electronic structure. The electric-double-layer capacitance (C_{dl}) value, which is positively correlated with the electrochemical surface area (ECSA), indicated that both $LaNi_5$-H-100th and $LaNi_5$-H-1st possessed the larger C_{dl} value (0.024 and 0.019 mF cm^{-2}, respectively) as compared to $LaNi_5$-F (0.010 mF cm^{-2}) (Figure S14, Supporting Information). This signified that the amount of potential active surface for $LaNi_5$ was substantially improved by hydrogenation and dehydrogenation cycles and could be ascribed to the hydrogen-induced lattice defects, grain refinement, and particle cracks.

To acquire in-depth insight into the excellent OER performance, the phase composition, morphology, and microstructure for $LaNi_5$-H-100th/FTO during OER were examined. First, we characterized intermetallic $LaNi_5$-H-100th without activation toward OER by in situ Raman spectra. The Raman spectra in the forward scanning direction exhibited the gradual increase of the Ni—O bond signals positioned at ≈475 and 558 cm^{-1} (**Figure 5**a), respectively, which could be due to the formation of γ-NiOOH that bear the highly intrinsic OER catalytic activity.[44,45] Specifically, the band at ≈475 cm^{-1} was related to the depolarized E_g mode (bending vibration of the oxygen atoms along the plane), whereas the peak positioned at ≈558 cm^{-1} was due to the polarized A_{1g} mode (stretching vibration of oxygen atom perpendicular to the plane) (Figure S15, Supporting Information).[15,46] The intensity ratio of E_g to A_{1g} peak was ≈1.37, implying the presence of lattice defects in the γ-NiOOH phase.[45,46] Meanwhile, the characteristic signals (A_g

and E_{2g} translatory modes at ≈281 and 336 cm^{-1}, respectively) belonging to $La(OH)_3$ could also be identified for $LaNi_5$-H-100th during alkaline OER.[47,48] On the other hand, the in situ Raman spectra during the OER process were also carried out for $LaNi_5$-F, and the results suggested a similar phase evolution to that of $LaNi_5$-H-100th/FTO (Figure S16, Supporting Information), that is, the generation of $La(OH)_3$ and γ-NiOOH on the surface. Nonetheless, compared with $LaNi_5$-H-100th, the characteristic peaks assigned to $La(OH)_3$ and γ-NiOOH were only apparently observed at 1.4 V, which lags behind that of LaNi-H-100th (1.3 V), implying the faster phase reconstruction of hydrogen-processed $LaNi_5$ during OER. Next, we investigated the phase and microstructure of $LaNi_5$-H-100th/FTO after the chronoamperometry (CA) test (OER at 1.53 V vs reversible hydrogen electrode (RHE)) ($LaNi_5$-H-100th/FTO-CA). The CA curve showed that the activity was basically unchanged at the constant potential for 24 h (Figure 5b), demonstrating exemplary stability during the OER. Interestingly, according to the XRD pattern after CA, in addition to the SnO_2 phase, only the $LaNi_5$ phase was observed (Figure S17, Supporting Information). To clarify whether the amorphous and/or nanosized Ni/La-based (hydro)oxides were formed, quasi in situ XAS spectra for $LaNi_5$-H-100th/FTO before and after CA were further measured and are compared in Figure 5c–f. As shown in Figure 5c, the Ni *K*-edge XANES spectra indicated an increased oxidation state (+1.9) for the Ni species in $LaNi_5$-H-100th/FTO-CA while the corresponding Ni *K*-edge EXAFS spectra verified the $LaNi_5$ phase structure for $LaNi_5$-H-100th/FTO (Figure 5d; Table S5, Supporting Information). Compared to this, the corresponding Ni *K*-edge EXAFS spectra for $LaNi_5$-H-100th/FTO-CA showed that in addition to the $LaNi_5$ phase structure, the apparent Ni−O bond and Ni−Ni bond belonging to the γ-NiOOH phase were also identified (Figure 5d; Table S5, Supporting Information), confirming the co-existence of $LaNi_5$ and γ-NiOOH via the phase transformation. To further support this point, a difference curve was achieved by subtracting the Ni *K*-edge EXAFS spectrum FT amplitude of $LaNi_5$-H-100th/FTO from that of $LaNi_5$-H-100th/FTO-CA (dotted green curve in Figure 5d). As expected, two peaks identified in the difference curve were matched very well with the Ni−O bond with a distance of 1.87 Å and the Ni−Ni bond with a distance of 2.83 Å in the γ-NiOOH phase (Table S5, Supporting Information), respectively, suggesting the formation of Ni-O(H) and edge-sharing Ni–Ni moieties after CA. In analogy to the Ni case, the comparison of XANES spectra of La *L*-edge in $LaNi_5$-H-100th/FTO before and after CA suggested an increased oxidation state (Figure 5e). The corresponding EXAFS of La *L*-edge in $LaNi_5$-H-100th/FTO-CA showed clearly that in addition to the La−Ni bond of the $LaNi_5$ phase, the La−O bond belonging to a $La(OH)_3$ phase was strikingly intensified (Figure 5f; Table S6, Supporting Information). These findings corroborated again the formation or increase of nickel oxyhydroxide and lanthanum hydroxide after CA. As another compelling evidence, the XPS spectra for $LaNi_5$-H-100th before and after CA changed dramatically, in which, the oxidation state for both La and Ni on the surface of the sample was increased to a +3 valence state after CA (more details can be found in Figure S18, Supporting Information). According to the Pourbaix diagram,[36] it is expected that La should theoretically be transformed to $La(OH)_3$ while Ni restructures itself in the form of Ni-oxyhydroxide under alkaline OER conditions, which was indeed consistent with the above observations. Because the amount of Fe species from the electrolyte probably has an important role in affecting the OER activity of Ni-based electrocatalysts,[49] the atomic ratio of Fe to Ni species was thus determined in the reconstructed phase after CA (Table S2, Supporting Information). It was found that a very small amount of Fe was deposited onto the electrode (the molar ratio between Fe and Ni was 0.006:1), which originated from the unpurified electrolyte. Thus, the high activity and stability of the active phase can majorly be ascribed to the Ni species. This point could also be supported by the nearly overlapping LSV curves of $LaNi_5$-H-100th/FTO electrode in Fe unpurified and purified KOH solution (Figure S19, Supporting Information).

From the FESEM results, it was evident that the particle surface of $LaNi_5$-H-100th becomes much more porous and a number of nanoparticles were generated after the OER durability test (**Figure 6**a,b), which indeed confirms the phase reconstruction in the OER process. Inductively coupled plasma spectrometry (ICP) analysis suggested that the atomic ratio of La to Ni in $LaNi_5$-H-100th changed from 1:5.0 before OER to 1:4.98 after OER (Table S2, Supporting Information), signifying that both La and Ni species were basically retained in the overall structure. The 3D morphology image by secondary-electron-excited scanning TEM (SE-STEM) further corroborated that a large number of nanoparticles were embedded within the bulk surface (Figure 6c), and the uniform bright field in the HAADF image exhibited the homogeneous distribution of metal species within the whole particle region (Figure 6d). Supporting this observation, the HRTEM image distinctly depicted the embedding of ultrafine nanocrystals within the matrix (Figure 6e). The identification of the corresponding lattice distances clearly showed that the nanocrystals were composed of the γ-NiOOH phase, as demonstrated by the lattice distance (0.211 nm) of the (105) facet of the γ-NiOOH phase (Figure 6f). Meanwhile, the nanodomains located on the boundary of γ-NiOOH nanoparticles were assigned to the $La(OH)_3$ phase, as marked by the lattice distance (0.319 nm) of the (101) facet of the $La(OH)_3$ phase (Figure 6g). The high-resolution elemental distribution results substantiated again that the signal of Ni was mainly distributed within particles while that of La was distributed on the boundary of these nanoparticles (Figure 6h–l), which was visibly different from that of samples before OER CA (Figure S20, Supporting Information). Moreover, the signal of O species was evenly distributed throughout the whole region (Figure 6k). These facts further strongly confirm that in the OER process, La behaves very differently from that of lean metals and metalloids and does not undergo dissolution but transforms as $La(OH)_3$ film on the outermost surface of the particles. Under the same conditions, the Ni converts into the active γ-NiOOH nanoparticles on the surface, resulting in the porously coupled structure that covers the remaining internal part of $LaNi_5$. To have a direct correlation, we further compared the electrochemical activity and stability of $LaNi_5$-H-100th to that of Ni-H-100th powder deposited on FTO electrode (Ni-H-100th/FTO) with the same mass loading in identical conditions. From the comparison, it was clear that Ni-H-100th/FTO exhibits a gradually decreased OER activity and stability (Figures S21 and S22, Supporting Information). The morphology change for Ni-H-100th

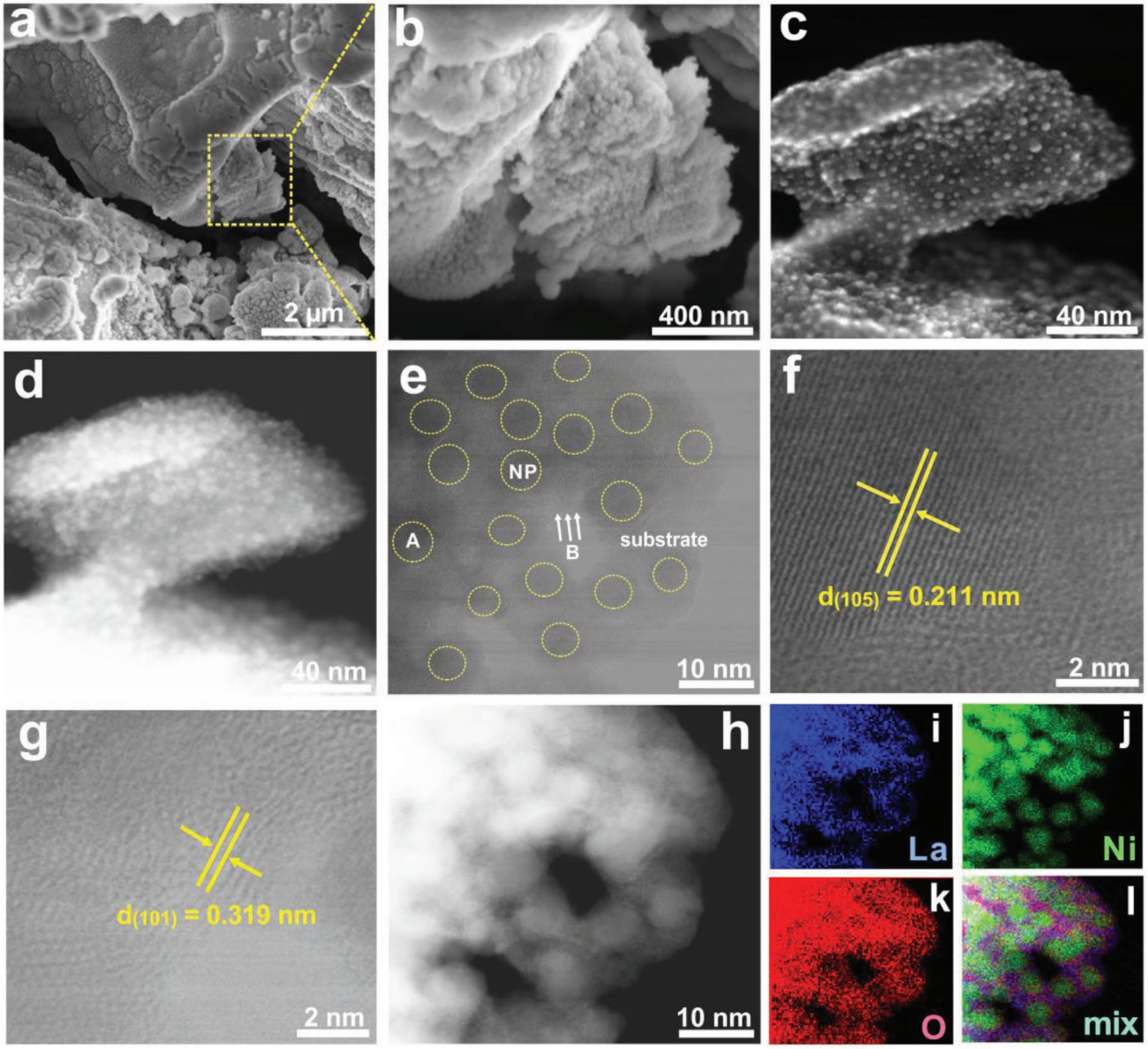

Figure 6. a,b) FESEM images of $LaNi_5$-H-100th after OER CA. c) SE-STEM image of $LaNi_5$-H-100th after OER CA and d) corresponding HAADF pattern. e) HRTEM image of $LaNi_5$-H-100th after OER CA and f,g) corresponding magnified images from zone A and zone B in (h), together with i–l) corresponding HAADF pattern and elemental mappings of La (i), Ni (j), O (k), and mixed species (l).

particles after OER CA was hard to be identified by FESEM (Figure S23, Supporting Information), suggesting that the reconstruction possibly only occurred on the surface. Further HRTEM results confirmed that instead of forming γ-NiOOH nanoparticles, a very thick amorphous layer was formed on the surface of Ni-H-100th after OER CA (Figure S24, Supporting Information), which could be assigned to the γ-NiOOH phase.[45] The SAED pattern for Ni-H-100th after OER CA also showed the broadened diffraction ring albeit the Ni phase was identified, confirming the generation of an amorphous phase on the surface. The agglomeration of the reconstructed active γ-NiOOH phase and/or the dissolution of Ni species might be the reason responsible for its activity decay under operating OER conditions.[50] This different observation implied that the presence of La could promote the formation of porously active γ-NiOOH nanoparticles.

On the other hand, to further confirm the positive effect of $La(OH)_3$ on the OER of NiOOH, density functional theory (DFT) calculations were carried out on pristine NiOOH and $NiOOH/La(OH)_3$ heterophase for OER. Previous theoretical calculation results have revealed that the oxygen site behaved more actively than the Ni site in the γ-NiOOH phase during OER.[51] Based on this finding, the NiOOH (001) layer with oxygen atom exposure was built as the theoretical model for calculation (Figure S25, Supporting Information). Correspondingly, a heterointerface was built by coupling the NiOOH (001) layer with $La(OH)_3$ (001). The (001) facet is selected due to the fact that it is the most stable surface in NiOOH for OER catalysis,[51]

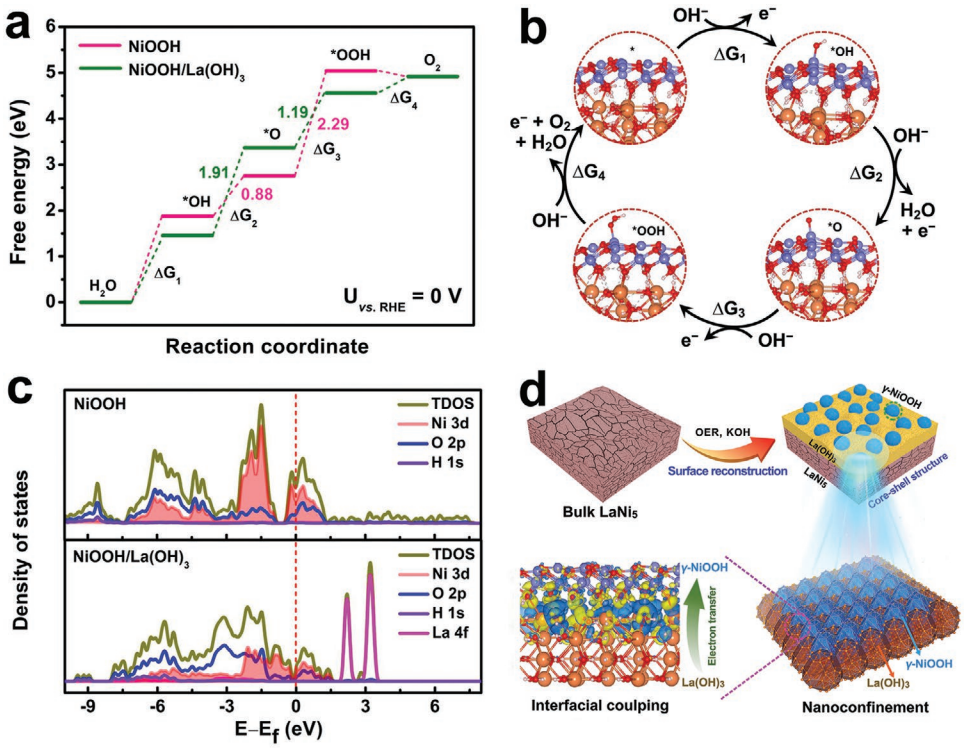

Figure 7. a) Free energy diagrams of alkaline OER at 0.0 V (vs RHE) for NiOOH and NiOOH/$La(OH)_3$. b) OER pathways based on the active Ni site of NiOOH/$La(OH)_3$ in alkaline media. c) The projected density of states (DOS) for NiOOH and NiOOH/$La(OH)_3$. d) Schematic illustration for the role of La in enhancing the OER performance of $LaNi_5$ precatalyst. Atoms with purple, yellow, red, and pink colors represent Ni, La, O, and H atoms, respectively. Isosurface with yellow and blue color represents the positive charge and negative charge accumulation.

and in order to better construct the heterointerface by using two complex hexagonal-type phases, the $La(OH)_3$ (001) layer was selected to match with NiOOH (001) layer. The OER energetics on these two systems have been carefully calculated by DFT (**Figure 7**a; Table S7, Supporting Information). As shown in Figure 7a, the potential-determining step for NiOOH was the transformation of *—O to *—OOH (* represents the active site), delivering an adsorption free energy barrier of 2.29 eV under the potential of 0 V vs RHE, which corresponds to an adsorption free energy barrier of 1.06 eV under the potential of 1.23 V vs RHE for OER. Compared to this, upon coupling with $La(OH)_3$, the potential-determining step was changed to the transformation of *—OH to *—O, which delivered a remarkable decrease of adsorption free energy barrier from 2.29 to 1.91 eV under the potential of 0 V vs RHE (0.68 eV under the potential of 1.23 V vs RHE) (Figure 7a), signifying the improvement of intrinsic OER activity by $La(OH)_3$. Intriguingly, upon the presence of $La(OH)_3$, the layer structure of NiOOH was slightly varied, together with the increase of the d-band center for Ni species from −2.35 eV for NiOOH to −2.25 eV for NiOOH/$La(OH)_3$, meaning the improved OER activity, and the active site was thus changed as Ni metal site (Figure 7b). The density of state (DOS) profiles for NiOOH and NiOOH/$La(OH)_3$ are also provided in Figure 7c. Being consistent with the previous reports,[51–53] the NiOOH layer had no bandgap, even when it was coupled with $La(OH)_3$ heterophase, suggesting the favorable charge transfer ability for these two systems during electrocatalysis. The difference in charge density distribution also showed the electron transfer from $La(OH)_3$ to the NiOOH layer (Figure 7d), confirming the strong interfacial charge interaction between these two subunits.

According to the above analysis, La could play the following roles in the OER catalytic process, as schematically outlined in Figure 7d: i) the presence of La could effectively contribute to the formation of porously active γ-NiOOH nanoparticles during alkaline OER; ii) La species in situ precipitate along the grain boundary, form hydroxide phase and inhibit the agglomeration of the transformed active γ-NiOOH nanodomains, which is presumed to expose more active sites and enhance the structural stability, thereby displaying exceptional durability; iii) the unreacted La remained in $LaNi_5$ continued to maintain the conductive properties of intermetallics core, thus promoting the charge transfer in the OER process; iv) at the same time, $La(OH)_3$ nanofilm provided the electron interplay with γ-NiOOH nanodomains, which was conducive to regulate the intrinsic OER activity of γ-NiOOH.

Inspired by the exceptional activity on FTO, Ni-H-100th, $LaNi_5$-H-100th, $LaNi_5$-H-1st, and $LaNi_5$-F powder were further deposited on NF which is currently a popular choice of substrates for OER because of its porosity, high conductivity, and large surface area. Both the phase structure and morphology of these materials could be retained after the electrodeposition process on NF (Figures S26 and S27, Supporting Information). Similar to that of FTO, the linear polarization curve showed poor activity for $LaNi_5$-F/NF, which delivered the overpotentials of 324 mV and 426 mV (η_{100}) at 10 and 100 mA cm^{-2}, respectively (**Figure 8**a). Remarkably, only after one cyclic hydrogenation and dehydrogenation treatment, the overpotential was

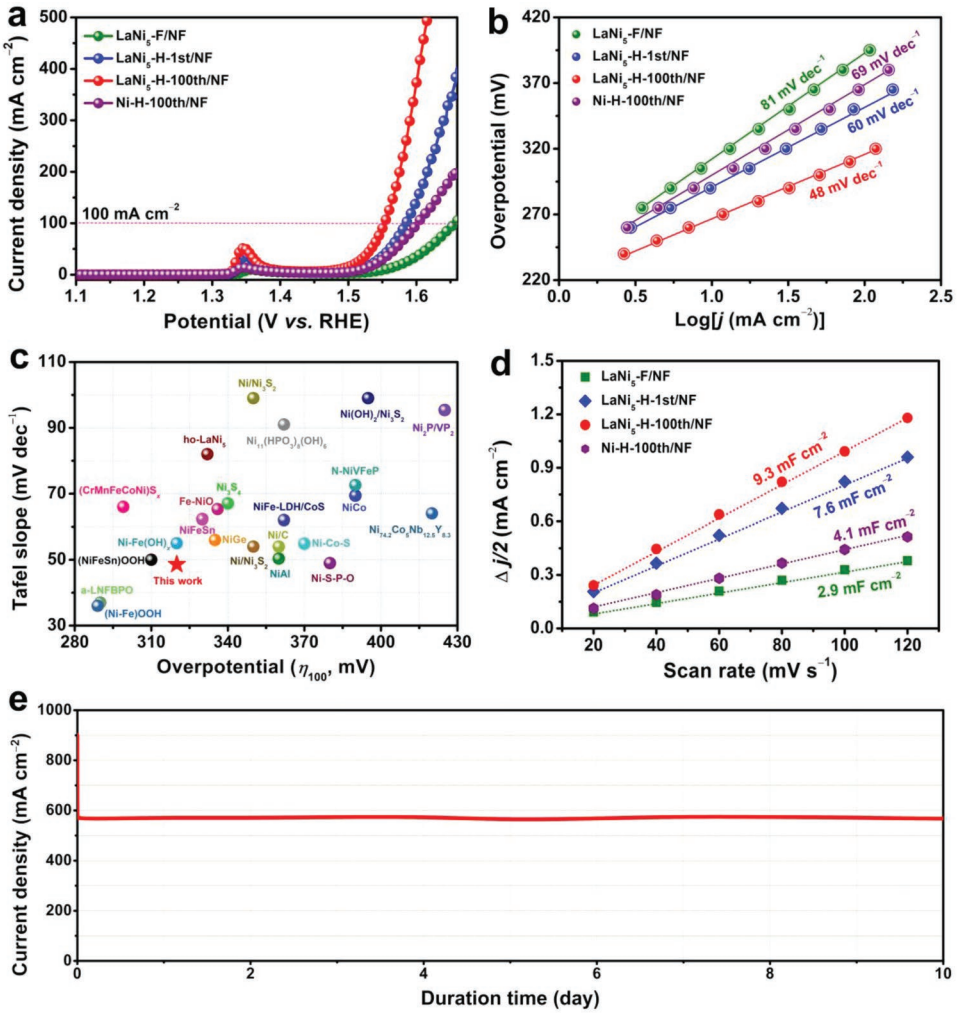

Figure 8. a) LSV curves and b) Tafel slopes of $LaNi_5$-F/NF, $LaNi_5$-H-1st/NF, $LaNi_5$-H-100th/NF, and Ni-H-100th/NF electrodes in 1.0 M KOH. c) Comparison of the activity of $LaNi_5$-H-100th/NF electrode with recently reported NF-supported Ni-based electrodes. d) C_{dl} values of $LaNi_5$-F/NF, $LaNi_5$-H-1st/NF, $LaNi_5$-H-100th/NF, and Ni-H-100th/NF electrodes. e) Durability curve of $LaNi_5$-H-100th/NF electrode at the potential of 1.64 V vs RHE.

reduced by 41 mV at 10 mA cm^{-2}, and it was further decreased to 254 mV after 100 cycles. Especially, such an activity optimization tendency was more apparent at 100 mA cm^{-2} or larger current densities, that is, an overpotential of 426, 354, and 322 mV was required to reach the current density of 100 mA cm^{-2} for $LaNi_5$-F/NF, $LaNi_5$-H-1st/NF, and $LaNi_5$-H-100th/NF, respectively. The overpotential at 100 mA cm^{-2} for $LaNi_5$-H-100th/NF was also lower than that of Ni-H-100th/NF (371 mV). Note that the pristine NF exhibited poor OER activity (Figure S28, Supporting Information), indicating its small contribution to the overall activity. The steady-state Tafel slopes also followed the same trend as FTO where a value of 48 mV dec^{-1} resulted for $LaNi_5$-H-100th which was smaller than those of $LaNi_5$-F (81 mV dec^{-1}), $LaNi_5$-H-1st (60 mV dec^{-1}) and Ni-H-100th (69 mV dec^{-1}) (Figure 8b). Notably, the OER activity of $LaNi_5$-H-100th attained in this work was significantly better compared to the commercial RuO_2/NF (Figure S28, Supporting Information), as well as the most of previously reported intermetallics and nickel-based electrocatalysts on NF (Figure 8c; Table S8, Supporting Information), rendering them one of the promising electrodes for practical application. In addition to this, the EIS spectra (Figure S29, Supporting Information) and C_{dl} values (Figure 8d; Figure S30, Supporting Information) on NF were also measured and are in accordance with the results obtained on FTO, highlighting again the advantage of hydrogen cycling strategy in improving OER activity.

As the durability at large current density is another indispensable factor for evaluating the practical application ability of an electrocatalyst, we, therefore, examined the stability of $LaNi_5$-H-100th at current densities higher than 500 mA cm^{-2} under alkaline conditions. As anticipated, the $LaNi_5$-H-100th deposited on NF showed basically unchanged exceptional long-term stability at a current density of ≈560 mA cm^{-2} for 10 days (Figure 8e). Notably, even under such a high current density and a long duration of time, the $LaNi_5$ phase and hierarchical structure still could be maintained well (Figures S31 and S32, Supporting Information). It should be mentioned that $LaNi_5$ has also been demonstrated to be an exceptional HER electrocatalyst,[30] thus an attempt was also made to deploy $LaNi_5$-H-100th as a bifunctional electrocatalyst for

overall water splitting. As depicted in Figure S33a,b (Supporting Information), the overpotentials to drive 100 mA cm^{-2} for HER and overall water splitting were ≈260 and 613 mV, respectively. Moreover, it could maintain the current density of ≈580 mA cm^{-2} for 120 h with only a little activity decay (Figure S34, Supporting Information). It is well known that the OER activity of a precatalyst is highly dependent on the composition, which greatly affects the reconstructed microstructure. Based on this point, the compositional engineering strategy can be considered for rare earth-TM-based electrocatalysts for the further optimization of OER performance. For example, the highly active Co, Fe, and Mn species can be incorporated into $LaNi_5$ to trigger the synergistic catalysis effect with Ni for OER; while the In, Ge, and Si species with easy leaching nature can also be considered to concurrently incorporate into $LaNi_5$ to accelerate their porous phase reconstruction during OER, and thereby increasing both the amount of surface active sites and mass transfer ability.

3. Conclusion

We have tackled the research questions successfully as mentioned in the introduction. To clarify whether and how hydrogen processing influences the OER performance of $LaNi_5$, the OER activity of bulk $LaNi_5$ before and after hydrogen processing was systematically compared by electrochemical routes, and it was discovered that the evolution of morphology and microstructure induced by hydrogen cycling could effectively revive the OER activity of bulk $LaNi_5$ with a decrease in overpotentials as high as ≈100 mV at 100 mA cm^{-2}. Following this observation, several advanced techniques including in situ Raman, quasi in situ XAS, SE-STEM as well as other ex situ approaches were applied to unequivocally unveil the positive roles of La in enhancing OER activity including the promotion effect for the formation of active γ-NiOOH nanoparticles, inhibition of the aggregation of γ-NiOOH nanoparticles, preservation of the inner core with conductivity as well as the optimization of free adsorption energy toward surface-bound intermediates. To the best of our knowledge, this is the first time a hydrogen processing strategy has been utilized to activate the OER activity of hydrogen storage intermetallics for hydrogen production, which embodies the concept of recycling hydrogen economy. The findings in this contribution also provide new insights into the OER mechanism of novel rare-earth TM-based intermetallics and will inspire the technological design of highly active, inexpensive, durable electrocatalysts.

Supporting Information

Supporting Information is available from the Wiley Online Library or from the author.

Acknowledgements

This work was supported by National MCF Energy R&D Program of China (2018YFE0306105), National Natural Science Foundation of China (52201269, 51972216), Natural Science Foundation of Jiangsu Province (BK20210735), Natural Science Foundation of the Higher Education Institutions of Jiangsu Province (21KJB430043), Collaborative Innovation Center of Suzhou Nano Science & Technology, the 111 Project, Suzhou Key Laboratory of Functional Nano & Soft Materials and Jiangsu Key Laboratory for Advanced Negative Carbon Technologies. Z.C. gratefully acknowledges the funding from Alexander von Humboldt (AvH) Foundation and Gusu leading talent plan for scientific and technological innovation and entrepreneurship (ZXL2022487). H.Y. thanks China Scholarship Council (CSC) for the Ph.D. fellowship. P.W.M. greatly acknowledges support from the German Federal Ministry of Education and Research in the framework of the project Catlab (03EW0015A/B). P.W.M. and M.D. acknowledge German Federal Ministry of Education and Research (BMBF project "PrometH2eus", 03HY105C).

Open access funding enabled and organized by Projekt DEAL.

Conflict of Interest

The authors declare no conflict of interest.

Data Availability Statement

The data that support the findings of this study are available from the corresponding author upon reasonable request.

Keywords

heterostructures, hydrogen storage intermetallics, oxygen evolution reaction, phase reconstruction, rare-earth metals

Received: September 11, 2022
Revised: December 5, 2022
Published online: February 1, 2023

[1] M. Yu, E. Budiyanto, H. Tüysüz, *Angew. Chem., Int. Ed.* **2022**, *61*, e202103824.
[2] C. Lee, K. Shin, C. Jung, P. Choi, G. Henkelman, H. Lee, *ACS Catal.* **2020**, *10*, 562.
[3] M. Görlin, P. Chernev, J. Ferreira de Araújo, T. Reier, S. Dresp, B. Paul, R. Krähnert, H. Dau, P. Strasser, *J. Am. Chem. Soc.* **2016**, *138*, 5603.
[4] S. L. Zhang, B. Y. Guan, X. F. Lu, S. B. Xi, Y. H. Du, X. W. Lou, *Adv. Mater.* **2020**, *32*, 2002235.
[5] Z. Chen, H. Yang, Z. Kang, M. Driess, P. W. Menezes, *Adv. Mater.* **2022**, *34*, 2108432.
[6] Y. Huang, S. L. Zhang, X. F. Lu, Z. P. Wu, D. Y. Luan, X. W. Lou, *Angew. Chem., Int. Ed.* **2021**, *60*, 11841.
[7] L. J. Zhang, W. W. Cai, N. Z. Bao, H. Yang, *Adv. Mater.* **2022**, *34*, 2110511.
[8] J. Song, C. Wei, Z. F. Huang, C. Liu, L. Zeng, X. Wang, Z. J. Xu, *Chem. Soc. Rev.* **2020**, *49*, 2196.
[9] Y. F. Zhao, X. F. Lu, G. L. Fan, S. Y. Luan, X. J. Gu, X. W. Lou, *Angew. Chem. Int. Ed.* **2022**, *61*, e202212542.
[10] B. Chakraborty, R. Beltrán-Suito, J. N. Hausmann, S. Garai, M. Driess, P. W. Menezes, *Adv. Energy Mater.* **2020**, *10*, 2001377.
[11] H. Shi, Y. T. Zhou, R. Q. Yao, W. B. Wan, X. Ge, W. Zhang, Z. Wen, X. Y. Lang, W. T. Zheng, Q. Jiang, *Nat. Commun.* **2020**, *11*, 2940.
[12] J. S. Mondschein, K. Kumar, C. F. Holder, K. Seth, H. Kim, R. E. Schaak, *Inorg. Chem.* **2018**, *57*, 6010.
[13] J. Zheng, J. Zhang, L. Zhang, W. Zhang, X. Wang, Z. Cui, H. Song, Z. Liang, L. Du, *ACS Appl. Mater. Interfaces* **2022**, *14*, 19524.

[14] X. Qiao, H. Kang, Y. Li, K. Cui, X. Jia, X. Wu, W. Qin, *Appl. Catal. B* **2022**, *305*, 121034.
[15] P. W. Menezes, S. Yao, R. Beltrán-Suito, J. N. Hausmann, P. V. Menezes, M. Driess, *Angew. Chem., Int. Ed.* **2021**, *60*, 4640.
[16] P. W. Menezes, C. Walter, J. N. Hausmann, R. Beltrán-Suito, C. Schlesiger, S. Praetz, V. Y. Verchenko, A. V. Shevelkov, M. Driess, *Angew. Chem., Int. Ed.* **2019**, *58*, 16569.
[17] J. N. Hausmann, R. Beltrán-Suito, S. Mebs, V. Hlukhyy, T. F. Fässler, H. Dau, M. Driess, P. W. Menezes, *Adv. Mater.* **2021**, *33*, 2008823.
[18] H. Sun, S. Song, X. Xu, J. Dai, J. Yu, W. Zhou, Z. Shao, W. Jung, *Adv. Energy Mater.* **2021**, *11*, 2101937.
[19] K. L. Svane, J. Rossmeisl, *Angew. Chem. Int. Ed.* **2022**, *61*, e202201146.
[20] R. Beltrán-Suito, V. Forstner, J. N. Hausmann, S. Mebs, J. Schmidt, I. Zaharieva, K. Laun, I. Zebger, H. Dau, P. W. Menezes, *Chem. Sci.* **2020**, *11*, 11834.
[21] J. N. Hausmann, R. A. Khalaniya, C. Das, I. Remy-Speckmann, S. Berendts, A. V. Shevelkov, M. Driess, P. W. Menezes, *Chem. Commun.* **2021**, *57*, 2184.
[22] Q. Zhou, Q. Hao, Y. Li, J. Yu, C. Xu, H. Liu, S. Yan, *Nano Energy* **2021**, *89*, 106402.
[23] H. Y. Kim, S. H. Joo, *J. Mater. Chem. A* **2020**, *8*, 8195.
[24] R. R. Chen, G. Chen, X. Ren, J. Ge, S. J. H. Ong, S. Xi, X. Wang, Z. J. Xu, *Angew. Chem. Int. Ed.* **2021**, *60*, 25884.
[25] P. W. Menezes, C. Panda, S. Garai, C. Walter, A. Guiet, M. Driess, *Angew. Chem., Int. Ed.* **2018**, *57*, 15237.
[26] Y. Zhao, X. Liu, S. Zhang, W. Wang, L. Zhang, Y. Li, S. Han, G. Xu, *Intermetallics* **2020**, *124*, 106852.
[27] Q. Zhang, Z. Chen, Y. Li, F. Fang, D. Sun, L. Ouyang, M. Zhu, *J. Phys. Chem. C* **2015**, *119*, 4719.
[28] Y. Nakamura, K. Oguro, I. Uehara, E. Akiba, *J. Alloys Compd.* **2000**, *298*, 138.
[29] Y. Nakamura, R. C. Bowman, E. Akiba, *J. Alloys Compd.* **2004**, *373*, 183.
[30] Y. Wu, Y. Liu, K. Liu, L. Wang, L. Zhang, D. Wang, Z. Chai, W. Shi, *Green Energy Environ.* **2022**, *7*, 799.
[31] F. Yu, H. Zhou, Y. Huang, J. Sun, F. Qin, J. Bao, W. A. GoddardIII, S. Chen, Z. Ren, *Nat. Commun.* **2018**, *9*, 2551.
[32] X. Wang, W. Li, D. Xiong, D. Y. Petrovykh, L. Liu, *Adv. Funct. Mater.* **2016**, *26*, 4067.
[33] F. Song, K. Schenk, X. Hu, *Energy Environ. Sci* **2016**, *9*, 473.
[34] C. Lartigue, A. L. Bail, A. Percheron-Guegan, *J. Less-Common Met.* **1987**, *129*, 65.
[35] M. H. Mendelsohn, D. M. Gruen, A. E. Dwight, *Nature* **1977**, *269*, 45.
[36] P. Garnier, V. Joseph, R. Krachewski, *ECS Trans.* **2013**, *58*, 119.
[37] K. Sakaki, N. Terashita, H. Kim, E. Majzoub, A. Machida, T. Watanuki, S. Tsunokake, Y. Nakamura, E. Akiba, *J. Phys. Chem. C* **2014**, *118*, 6697.
[38] Z. Xia, S. Guo, *Chem. Soc. Rev.* **2019**, *48*, 3265.
[39] Y. Wang, P. Han, X. Lv, L. Zhang, G. Zheng, *Joule* **2018**, *2*, 2551.
[40] X. Cao, X. Yan, L. Ke, K. Zhao, N. Yan, *ACS Appl. Mater. Interfaces* **2021**, *13*, 22009.
[41] Y. Wang, C. Yang, Y. Huang, Z. Li, Z. Liang, G. Cao, *J. Mater. Chem. A* **2020**, *8*, 6699.
[42] V. E. Antonov, *J. Alloys Compd.* **2002**, *330–332*, 110.
[43] J. Binns, M. Donnelly, M. Wang, A. Hermann, E. Gregoryanz, P. Dalladay-Simpson, R. T. Howie, *Phys. Rew. B* **2018**, *98*, 140101.
[44] S. Y. Lee, I. S. Kim, H. S. Cho, C. H. Kim, Y. K. Lee, *Appl. Catal. B* **2021**, *284*, 119729.
[45] I. Mondal, J. N. Hausmann, G. Vijaykumar, S. Mebs, H. Dau, M. Driess, P. W. Menezes, *Adv. Energy Mater.* **2022**, *12*, 2200269.
[46] S. Lee, L. Bai, X. Hu, *Angew. Chem., Int. Ed.* **2020**, *59*, 8072.
[47] A. Subasri, K. Balakrishnan, E. R. Nagarajan, V. Devadoss, A. Subramania, *Electrochim. Acta* **2018**, *281*, 329.
[48] Q. Y. Mu, Y. D. Wang, *J. Alloys Compd.* **2011**, *509*, 2060.
[49] S. Loos, I. Zaharieva, P. Chernev, A. Lißner, H. Dau, *ChemSusChem* **2019**, *12*, 1966.
[50] J. R. Esquius, G. Algara-Siller, I. Spanos, S. J. Freakley, R. Schlögl, G. J. Hutchings, *ACS Catal.* **2020**, *10*, 14640.
[51] X. Ren, C. Wei, Y. Sun, X. Liu, F. Meng, X. Meng, S. Sun, S. Xi, Y. Du, Z. Bi, G. Shang, A. C. Fisher, L. Gu, Z. J. Xu, *Adv. Mater.* **2020**, *32*, 2001292.
[52] K. Wang, H. F. Du, S. He, L. Liu, K. Yang, J. M. Sun, Y. H. Liu, Z. Z. Du, L. H. Xie, W. Ai, W. Huang, *Adv. Mater.* **2021**, *33*, 2005587.
[53] B. Wu, S. Gong, Y. C. Lin, T. Li, A. Y. Chen, M. Y. Zhao, Q. J. Zhang, L. Chen, *Adv. Mater.* **2022**, *34*, 2108619.